

Rotating Stall Observations in a High Speed Compressor—Part II: Numerical Study

J. Dodds

Rolls-Royce,

Derby DE24 8BJ, UK

e-mail: John.dodds@rolls-royce.com

M. Vahdati

Imperial College,

London SW7 2AZ, UK

e-mail: m.vahdati@imperial.ac.uk

In this two-part paper the phenomenon of part span rotating stall is studied. The objective is to improve understanding of the physics by which stable and persistent rotating stall occurs within high speed axial flow compressors. This phenomenon is studied both experimentally (Part I) and numerically (Part II). The experimental observations reported in Part I are now explored through the use of 3D unsteady Reynolds-averaged Navier-Stokes (RANS) simulation. The objective is to both validate the computational model and, where possible, explore some physical aspects of the phenomena. Unsteady simulations are presented, performed at a fixed speed with the three rows of variable stator vanes adjusted to deliberately mismatch the front stages and provoke stall. Two families of rotating stall are identified by the model, consistent with experimental observations from Part I. The first family of rotating stall originates from hub corner separations developing on the stage 1 stator vanes. These gradually coalesce into a multicell rotating stall pattern confined to the hub region of the stator and its downstream rotor. The second family originates from regions of blockage associated with tip clearance flow over the stage 1 rotor blade. These also coalesce into a multicell rotating stall pattern of shorter length scale confined to the leading edge tip region. Some features of each of these two patterns are then explored as the variable stator vanes (VSVs) are mismatched further, pushing each region deeper into stall. The numerical predictions show a credible match with the experimental findings of Part I. This suggests that a RANS modeling approach is sufficient to capture some important aspects of part span rotating stall behavior.

[DOI: 10.1115/1.4028558]

Introduction

The phenomenon of rotating stall has been the subject of research for many decades. Significant progress has been made in this field through both analytical and experimental techniques, leading to the well-known *modal* and *spike* stall inception models [1–3].

Although 3D RANS methods have also been in use for some time, the significant computational effort required to model an unsteady process such as rotating stall has until recently been out of reach. Some progress has been made using “reduced order” models where some simplification is made, for example modeling just a 2D slice [4] or a partial annular sector [5,6].

More recently, the use of parallel computing techniques has allowed the rotating stall problem to be addressed using a full annulus model. Vahdati et al. [7] have made predictions of part span rotating stall in a high speed compressor, whilst Choi et al. [8] performed a similar investigation for a high speed fan, showing good agreement with experimental data [9]. Similar studies have also been performed by Gourdain et al. [10] and Chen et al. [11].

The use of CFD methods has had a significant impact on the physical understanding of rotating stall. Using a partial sector model, Vo et al. [12] proposed criteria for spike stall inception, related to the over-tip leakage. More recent numerical analysis has developed this further, showing that spike stall inception is quite possible at fixed-end blades, without over-tip leakage, on both axial [13] and centrifugal [14] compressors. Both investigations are backed by experiment [15,16].

In this paper, the objective is to build upon the experimental work presented in Part I, whereby rotating stall was triggered in a high speed compressor by deliberate mis-staggering of the VSVs. This investigation showed two distinct “families” of rotating stall, giving rise to high and low frequency signals when measured on casing mounted pressure transducers.

The primary objective of this second paper is to explore the capability of unsteady RANS methods for prediction of rotating stall. Full annulus unsteady analyses are therefore performed at conditions from Part I, allowing the CFD model to be validated. Where possible, the model is also used to provide a deeper insight into the experimental observations.

Description of Compressor Model

The test case used within this paper is identical to that presented in the experimental analysis of Part I. The research compressor was designed by Rolls Royce and is representative of a modern high speed machine. The compressor has eight stages with an inlet guide vane (IGV) upstream of the first rotor. The IGV and the first two stator rows (S1 and S2) are of variable stagger type. Tip clearances and stator shroud clearances are representative of a modern high speed compressor and the Rotor 1 relative inlet flow is supersonic at design conditions.

A schematic view of the test compressor is shown in Fig. 1(a), with the corresponding unsteady computational domain shown in Fig. 1(b). Based on the experimental observations, the unsteady, full annulus domain extends from the inlet through to Rotor 3 exit. Downstream of this location the flow was assumed steady, with a single passage mixing plane approach adopted. The validity of this assumption is tested in a later section.

A long duct was added upstream of the compressor to minimize any unphysical coupling between unsteadiness within the compressor and the inlet plane. A fully meshed choked nozzle was

Contributed by the International Gas Turbine Institute (IGTI) of ASME for publication in the JOURNAL OF TURBOMACHINERY. Manuscript received July 8, 2014; final manuscript received July 29, 2014; published online November 18, 2014. Editor: Ronald Bunker.

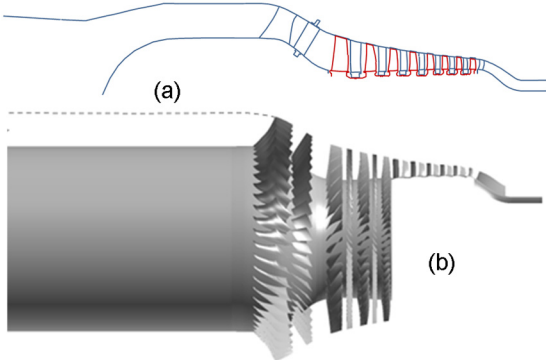


Fig. 1 A schematic view of (a) the test compressor and (b) the unsteady computational domain

used at the domain outlet allowing atmospheric conditions to be used at both inlet and exit. This nozzle was sized to achieve a part speed operating point consistent with the Part I experiment, remaining fixed throughout this investigation. Adjustments to the VSVs (IGV, Stator 1, and Stator 2) were achieved through a mesh deformation procedure.

The calculations presented in this paper were performed using a cell-vertex, time-marching RANS solver, utilizing the single equation Spalart–Allmaras turbulence model. This code has been used previously for rotating stall investigations on both high speed compressors [7] and fans [8], in the latter case showing results consistent with experimental data [9]. The domain was meshed using an unstructured grid within the blade to blade plane, with a structured grid in the radial direction consisting of 45 radial mesh points. In total, the computational domain shown in Fig. 1(b) consisted of approximately 70×10^6 nodes, with typically 0.3×10^6 nodes per passage. This resulted in a run-time of two days per shaft revolution using 64 CPUs. Steady single passage analyses were performed to confirm that the mesh was of adequate resolution, which is assumed to also be adequate for the unsteady model providing stall cells are of sufficiently large scale (greater than one blade passage).

The clearances between the rotor blades and the casing were set at a level consistent with the test rig, with five radial mesh points across the clearance gap. Fillets at the blade ends and leakage flows through the shroud cavities beneath the stator vanes were not included. However, steady analyses with these features included showed their relative importance to be outweighed by the effect of the VSVs.

Based upon the frequency of the phenomena observed in Part I, a temporal discretization level of 1200 time steps per shaft revolution was used. Convergence studies were undertaken at several conditions to confirm that the results were insensitive to this assumption.

Test Conditions Studied

All simulations were undertaken at 85% of design speed, on the experimental working line shown in Fig. 2. This speed was chosen based on the experiment which showed significant interesting activity at 85%. Also, the experiment consisted of slow accelerations rather than fixed speed throttling (as is attempted here numerically). However, the experimental acceleration rate was sufficiently slow that each speed can be assumed to be quasi-steady. It is therefore valid to compare any predictions of *stable* rotating stall with experimental data at 85% speed.

The stagger of the three VSV rows were configured differently for each simulation. As discussed in Part I, adjustment to the stagger of each of the three variable stator rows provoked stall in either the Rotor 1 or Stator 1/Rotor 2 regions. The experimental observations split the resulting behavior into the following two “families”:

- Stall of Stator 1/Rotor 2 gave rise to 4–6 cells. The casing pressure transducers exhibited a stable, well-defined spectral

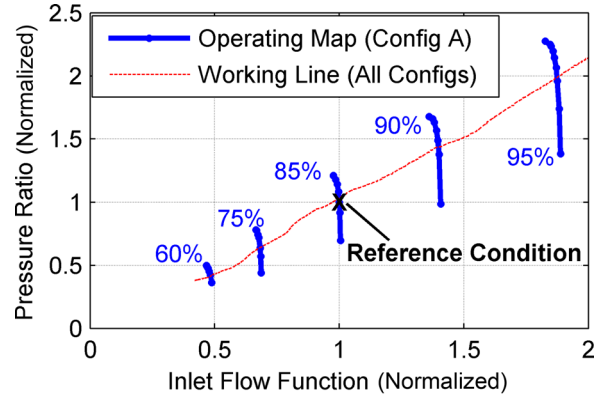


Fig. 2 Operating map for the test compressor

peak suggesting the stall cell pattern was uniform, although at certain speeds the number of cells (spatial mode order) changed almost spontaneously (see Part I, Fig. 7).

- Stall of Rotor 1 gave rise to over 10 cells. This exhibited multiple spectral peaks, suggesting some nonuniformity existed in the pattern of stall cells in both time and space (see Part I, Fig. 12). At certain conditions the cell length scale became comparable to that of the rotor blade pitch, resulting in a cut-on acoustic source.

Four configurations were chosen for numerical study, as shown in Table 1, which shows how the VSVs were configured relative to a chosen datum known as case “A.” The naming convention used in Part I is also used here. The observed experimental behavior for these configurations is also shown in Table 1. Cases “D” and “G” were the worst cases for the low and high stall cell count phenomena, respectively.

Some numerical difficulty was encountered during analysis of case D. Therefore, the level of “restagger” was reduced to 80% of the level tested in Part I—this case is denoted “D*”. An additional *untested* case was also created for convenience, with Stator 2 opened by 5 deg. This offloads the front stages such that no rotating stall would be expected. This has been denoted case “Z”.

Following the same methodology discussed in more detail in Part I, a simple meanline model was used to assess the effect of each configuration on the loading of Rotor 1, Stator 1, and Rotor 2 (these rows are most susceptible to stall when the variable vanes are adjusted). Figure 3 shows the results of this model when run for each configuration at the reference condition shown in Fig. 2. The Lieblein Diffusion Factor [17] was used as a means of comparing each case. It can be seen in Fig. 3(a) that the progression through configurations Z, A, and D* will stall Rotor 2, whilst Z, A, and G will stall Rotor 1. Figure 3(b) also shows that the Stator 1 loading correlates well to that of Rotor 2, implying that Stator 1 and Rotor 2 will tend to stall “as a pair”. The other configurations shown were tested during the experiment but are not investigated further in this paper.

Steady State Model Validation

In order to gain some confidence in the model, steady analyses were performed at 85% speed for case A. For the purposes of making a comparison with the model, the compressor rig was stabilized at 85% speed and the radial profiles of total pressure acquired from probes mounted upon the stator leading edges. A comparison between the model and the experiment is shown in Fig. 4 at both Stator 1 and Stator 2 leading edge.

The agreement at Stator 1 leading edge is satisfactory, with only slight deviation from experiment toward the casing. The agreement at Stator 2 leading edge is also good, where a “dip” in the total pressure profile at 25% span is captured by the model. The reason for this dip can be seen in the midpassage entropy contours in Fig. 5, showing a region of separation local to

Table 1 Adjustments made in model to VSVs and their effect relative to datum

Configuration	Amount of restagger			Experimental observations
	IGV	S1	S2	
A	0 deg	0 deg	0 deg	Weak activity <5EO (S1/R2 stall) Up to 81% speed, mode order 4 and weak activity >5EO (R1 stall) 80–87% speed
Z	0 deg	0 deg	-5 deg	Multiple mode orders 23–29 clearly visible Mode 28 dominant at 85% speed
D (D*)	+4.5 deg (+3.6 deg)	-3.5 deg (-2.8 deg)	+4.5 deg (+3.6 deg)	Not tested (no rotating stall expected) Strong activity <5EO (S1/R2 stall) Up to 91% speed Mode orders 4, 5, 6, 5 in sequence Mode 6 at 85% speed
G	-4.5 deg	+3.5 deg	+3.5 deg	Strong activity >5EO (R1 stall) Up to 91% speed Multiple mode orders. 13–16 clearly visible Mode 15 dominant at 85% speed

Note: *Denotes closure of vane away from axial.

Stator 1/Rotor 2 hub. A further separation can be seen at Rotor 1 tip. The sections that now follow investigate how these features develop using an *unsteady* modeling approach.

Effect of Stator 1/Rotor 2 Stalling

The effects of progressively pushing the Stator 1/Rotor 2 region into stall are now investigated by performing unsteady numerical simulations on configurations Z, A, and D* (see Fig. 3). The numerical strategy adopted was to initially run 5 shaft revolutions on configuration Z, in order to allow a realistic unsteady solution to develop *with minimal stall present*. This solution was then used as a starting point for analysis of the more stalled condition A. For

brevity, the details of the case Z solution are not presented here. With this solution obtained, the VSVs were then adjusted into their case A positions and the calculation resumed. This instant is defined herein as revolution zero.

Figure 6 shows how the solution for case A evolves transiently, in terms of axial velocity at Stator 1 exit, over the subsequent 10 shaft revolutions. This starts from the unstalled case Z solution. Initially, for the first half revolution, the flow is axisymmetric and the only circumferential disturbance is due to stator wakes. By 0.5 revolutions, blockage develops in the Stator 1 hub region, still in an axisymmetric manner. Subsequent to this, the blockage regions coalesce into multiple short lengthscale disturbances, rotating in the same sense as the shaft, with 17 discrete disturbances visible at $1\frac{1}{2}$ shaft revolutions. As the solution progresses, these

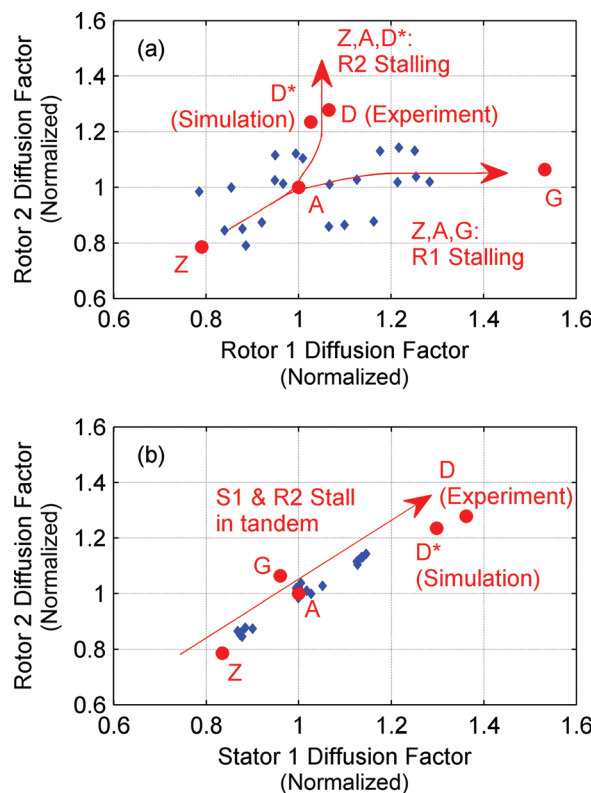


Fig. 3 Mean line assessment to “rank” the stalling effect of each configuration at a fixed inlet flow function

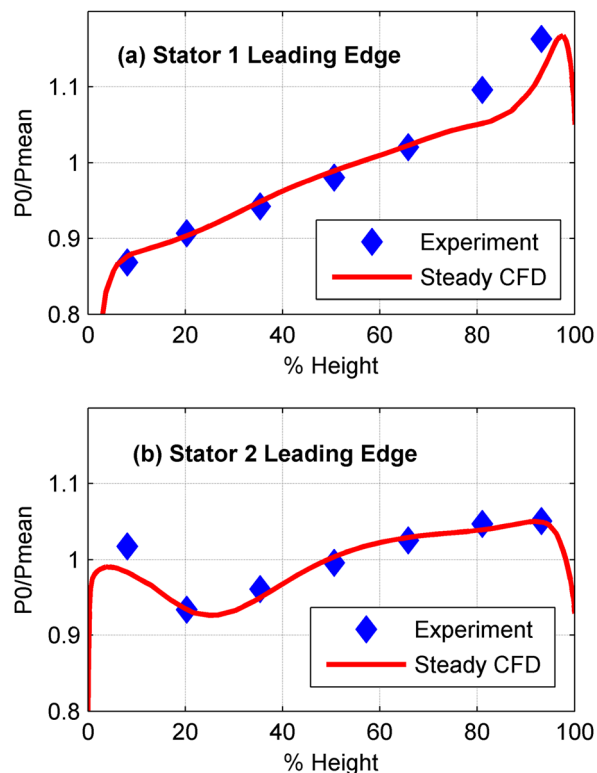


Fig. 4 Case A—total pressure profile

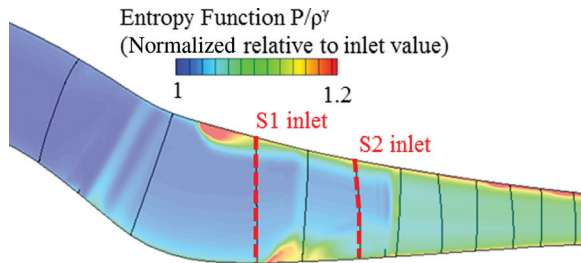


Fig. 5 Steady CFD for case A—mid passage entropy function

disturbances gradually merge together until the solution stabilizes naturally on a uniform pattern of 7 cells.

This transient process is also visualized, in Fig. 7, in terms of the circumferential profile of Stator 1 trailing edge axial velocity at 10% span. Initially, only horizontal (stationary) disturbances are present, i.e., the stator wakes. By 0.5 revolutions the vane passages fill with blockage until, by 1½ revolutions, traveling disturbances emerge. The gradual merging of these “stall cells” can then be observed over the next 10 revolutions until the calculation stabilizes on a 7 cell pattern, which propagates at 25% of the shaft rotational speed.

Once the configuration A simulation was stable and periodic, at approximately 12½ shaft revolutions, the variable vanes were moved again to represent configuration D*. Figures 8 and 9 show, in the same manner, how the 7 cell pattern reacts to the more stalled operating point (see Fig. 3).

Almost instantaneously the stall cells grow in size and accelerate (as evident in the change of slope in Fig. 9). Between revolution 14 and 15, merging of stall cells can be observed at two circumferential locations. The calculation eventually stabilizes on a pattern of 5 cells, propagating more rapidly at 40% of shaft rotational speed. The relationship between cell size and propagation speed is left for the discussion where the results will be considered alongside experimental data.

More detailed attention is now given to the process of stall cell formation in the first 2 shaft revolutions for case A. Whilst Figs. 6–9 clearly show rotating stall is present within the Stator 1 hub region, this does not directly imply that stall originates within the stationary vane.

In order to gain further insight into the origin of this behavior, circumferential profiles of static pressure were extracted around the annulus from the solution at 10% span, immediately upstream of Rotor 1, Stator 1, and Rotor 2. This was repeated at several instantaneous points during the transient in Fig. 7. These were then

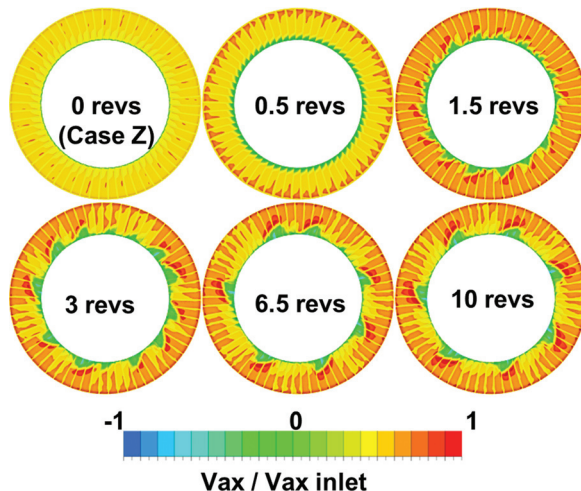


Fig. 6 Transient solution at S1 trailing edge, when vanes are moved from case Z to case A

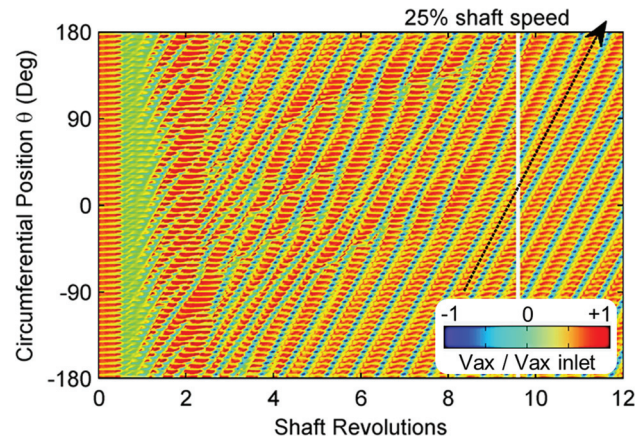


Fig. 7 Transient solution at S1 trailing edge, 10% span, when vanes are moved from case Z to case A

analyzed using a spatial Fourier transform to deduce the modal content within the flow—the resulting plots shown in Fig. 10.

Initially the solution (for case Z) has no stalled flow present, with the only visible modes due to the blades themselves and their harmonics, as labeled. By revolution 1, activity appears upstream of Stator 1 with a mode order of approximately one third that of the stator itself, corresponding to the 17 discrete features in Figs. 6 and 7. Importantly, this feature is *not* observed ahead of Rotor 1 or Rotor 2—it is only present upstream of Stator 1.

This suggests that circumferentially nonuniform flow structures (stall cells) are initially forming *within* Stator 1—their blockage effect resulting in a circumferential variation in upstream static pressure. This is further supported by a sharp fall in the amplitude of the pressure field associated with Stator 1 itself, to half of its original (unstalled) level, implying a breakdown in the periodic flow from one blade passage to the next. By revolution 1.6, the stalling mode has grown to have the same amplitude as Stator 1 itself, remaining weak at the other positions. The solution at revolution 12 is also shown. By this time the stall signal has grown in wavelength both axially and circumferentially, with mode seven becoming dominant at over twice the Stator 1 amplitude, clearly now also visible downstream at Rotor 2 leading edge.

This implies that rotating stall initially forms locally in Stator 1, with shorter circumferential lengthscale of mode order 17. The stall cells then grow axially and circumferentially and merge to stabilize at mode order 7.

The equivalent Fourier decomposition of static pressure for case D*, with 5 stall cells, is shown in Fig. 11, also at Stator 1 leading edge, 10% span. The dominant mode order is 5, consistent with 5 cells, with a first harmonic clearly visible. Modulation of the rotating stall with the Stator 1 signal is also evident in the form of sidebands.

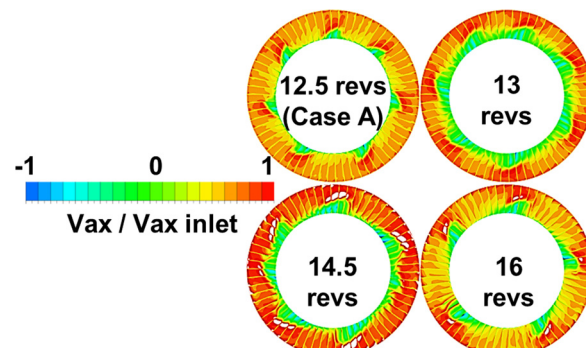


Fig. 8 Transient solution at S1 trailing edge, when vanes are moved from case A to case D*

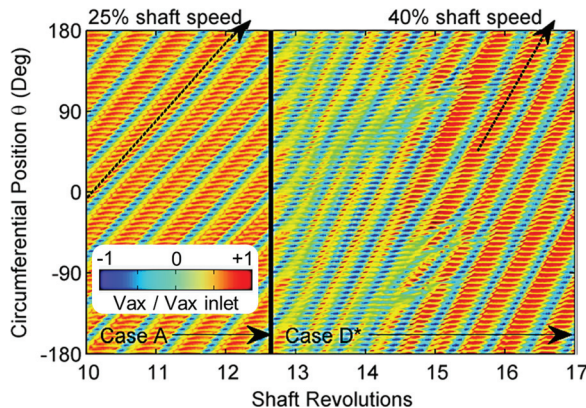


Fig. 9 Transient solution at S1 trailing edge, 10% span, when vanes are moved from case A to case D* (VSV adjustment denoted by solid black line)

The location of the stall cells is illustrated in Fig. 12, showing the final case D* solution at 20% span, across Rotor 1, Stator 1, and Rotor 2. One of the five stall cells is clearly visible as a region of axially reversed flow. The cell is dominant in the Stator 1 region, with 4 passages completely filled with reverse flow. The cell appears to lose its structure across the adjacent rotors, implying that the fully developed stall cell phenomenon resides primarily *within the stator*.

Using the modal analysis technique shown in Fig. 11, the axial and radial extent of the disturbance can be explored by determining the spatial modes at any axial/radial location. It should emphasize that a simplification is made here by considering only the static pressure perturbation induced by the stall cell, in order to allow comparison with experiment.

Figure 13 shows how the amplitude of the 5th mode varies along the hub and casing at the leading edge of each row. The peak intensity clearly occurs close to the hub, upstream of Stator 1, with the corresponding intensity at the casing less than half the hub level. Upstream, the disturbance is attenuated rapidly across Rotor 1 hub, which, at this condition, operates locally on a

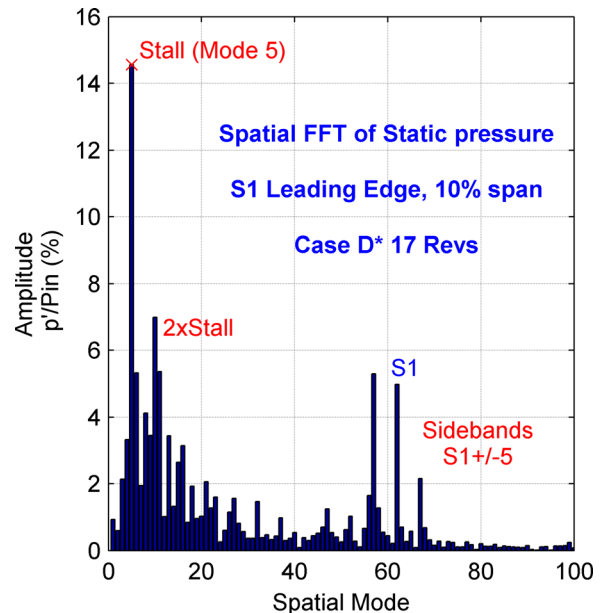


Fig. 11 Spatial modes (Stator 1)—case D*

negatively sloped characteristic. Consequently, the rotor hub does not itself stall in response to the exit static pressure variation (as seen in Fig. 12), preventing the stall cells from growing axially upstream into the Rotor 1 blade passages.

Downstream of this peak the hub static pressure variation is more gradually attenuated, with significant attenuation across the hub of Stator 1 itself, although the flow must still clearly have significant vortical content, as shown in the axial velocity contours at the stator trailing edge in Fig. 8.

Further downstream the disturbance is artificially terminated by the mixing plane at Rotor 3 exit. In order to confirm this modeling assumption, the calculation was repeated with the mixing plane moved one stage downstream to Rotor 4 exit. The corresponding axial distribution is also shown in Fig. 13. The solution also evolved into a pattern of 5 stall cells, implying the resulting behavior was not affected, with the resulting axial distribution showing only small differences.

The static pressure variation at the casing, also shown in Fig. 13, arises from the radial redistribution of flow around the cells at the hub, locally raising the velocity toward the casing (as can be seen in Fig. 8) and lowering the static pressure. It appears, from Fig. 13, that the casing peak occurs some distance downstream of that at the hub.

Comparison With Experiment. It is now possible to relate this observed behavior back to the experimental data shown in Part I.

For configuration D, experimental analysis of the casing pressure transducers and rotating strain gage spectra showed that, at 85% speed, a 6 cell rotating stall pattern was clearly present, rotating at half of the shaft speed (see Part I, Fig. 7). At a slightly higher speed of 86%, this transitioned spontaneously into a 5 cell

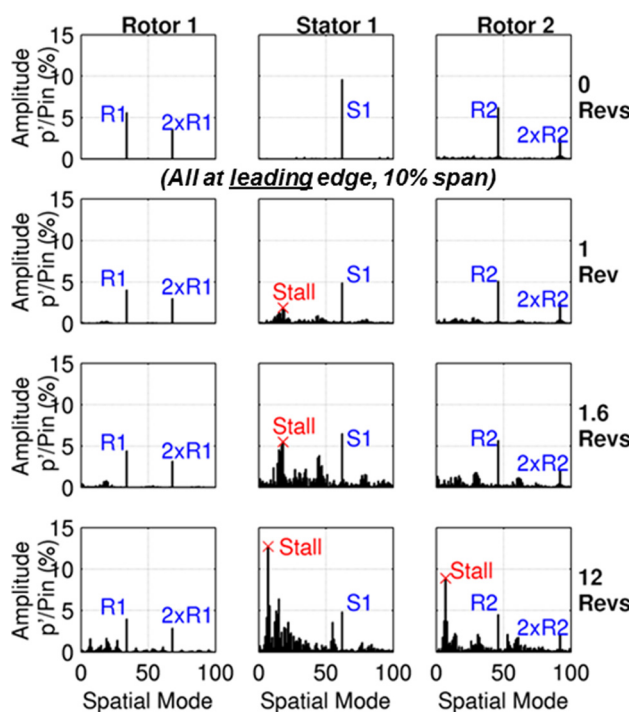


Fig. 10 Spatial modes observed as stall forms

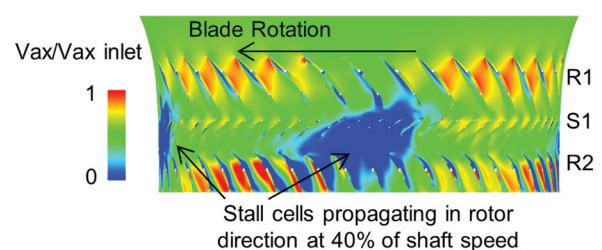


Fig. 12 Axial velocity field at 20% span—case D*

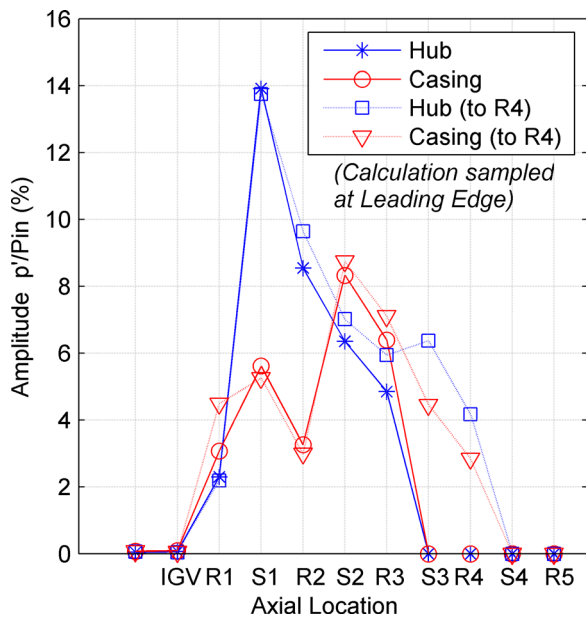


Fig. 13 Case D*-distribution of 5th mode (hub and casing)

pattern rotating at 55% of the shaft speed. Both experimental cases are therefore considered here for comparison.

The equivalent simulation for configuration D*, once stabilized, clearly predicts a 5 cell pattern rotating at a somewhat lower speed of 40% shaft speed. This gives some confidence that unsteady RANS simulations are capable of predicting part span rotating stall.

The predicted axial distribution of the disturbance is also compared with experiment in Fig. 14, by performing modal analysis similar to Fig. 13, now at the location of the casing pressure transducers, which are included as a subplot. Experimental data is included for both 85% and 86% speeds. The predicted axial distribution of the 5 cell disturbance agrees well with the experiment for the equivalent 5 cell stall at 86% speed. The peak intensity clearly occurs in the Stator 2/Rotor 3 gap (at location P3), despite the stall cell itself being present at the hub one whole stage further upstream.

In summary, this section shows that, as the VSVs are adjusted in order to stall Stator 1/Rotor 2, rotating stall cells form initially in the Stator 1 hub region, which coalesce into a coherent pattern of 7 cells. Pushing this region deeper into stall shows that the stall cells grow and accelerate, stabilizing on a pattern of 5 cells. Experimental observations are shown to support this finding.

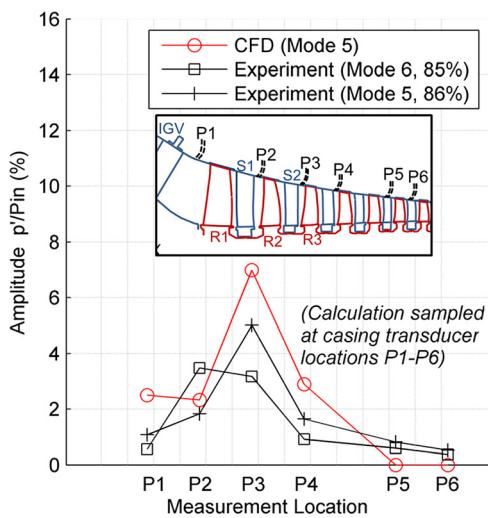


Fig. 14 Casing distribution case D* of stalling mode—comparison with experiment

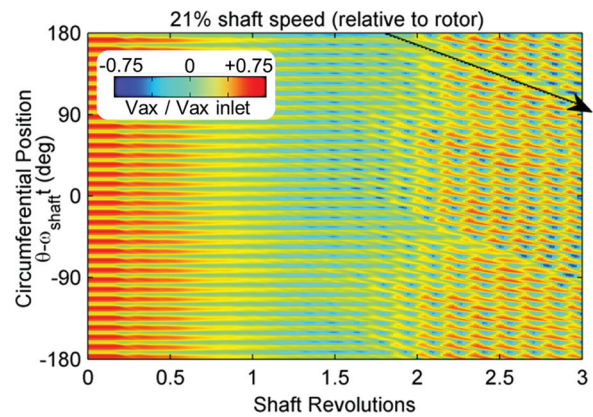


Fig. 15 Transient solution at R1 leading edge, 99% span, when vanes are moved from case Z to case A

Effect of Rotor 1 Stalling

Attention now focuses on the progression through configuration Z, A, and G—pushing Rotor 1 into stall (Fig. 3). Case A will be considered first and it should be noted that the case A solution here is identical to that presented in the previous section, Effect of Stator 1/Rotor 2 Stalling (i.e., stall is also forming at S1/R2 hub).

Figure 15 shows, for case A, how the axial velocity field develops around the circumference at 99% span, immediately upstream of Rotor 1 leading edge. This is shown in a frame of reference moving with the rotor, for the first 3 revolutions starting from the unstalled case Z.

Initially, the horizontal lines represent the periodic velocity field induced by each blade. Over the first revolution, the blade passages fill with blockage in an axisymmetric manner until, at around 1.5 revolutions, traveling disturbances become evident, at a speed corresponding to 79% of shaft speed (absolute frame). These disturbances are of lengthscale comparable to that of a rotor pitch.

Beyond the 3 revolutions shown in Fig. 15, some merging of the stall cells occurs, although they remain stable at this short lengthscale. In order to accurately determine the mode order of this disturbance once the calculation had stabilized at revolution 12, the circumferential profile of static pressure was extracted, also at 99% span, immediately upstream of Rotor 1. The Fourier transform of this profile is shown in Fig. 16, with a dominant

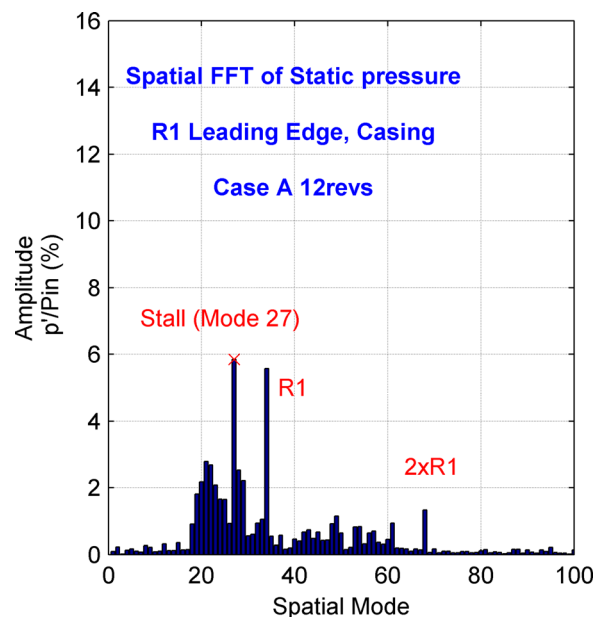


Fig. 16 Spatial modes (Rotor 1)—case A final

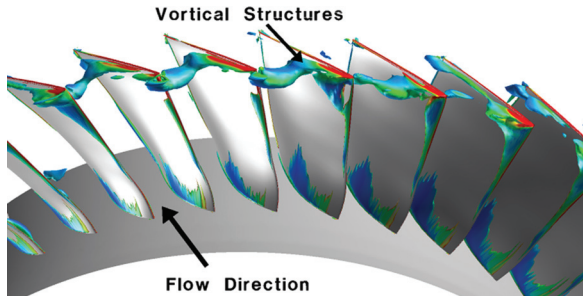


Fig. 17 Case A isosurface of λ_2 for R1

mode order of 27. At this point the propagation speed had stabilized at 73% of shaft speed.

In understanding the nature of these disturbances it is instructive to contrast these observations with other reported cases. Young et al. [15] showed experimentally the presence of similar stable disturbances, comparable to a blade pitch in scale. Unsteady RANS analysis of the stall inception process, performed by Pullan et al. [13], showed that these features could be explained by radial vortex like structures shedding from the blades as they stalled. These migrated across the passage, causing the adjacent blade to stall in the same manner, thus leading to a propagating disturbance.

Following, therefore, the same visualization method as Pullan et al. [13], a snapshot of the final case A solution is shown for Rotor 1 in Fig. 17, displaying an isosurface of the λ_2 vortex parameter for Rotor 1. Discrete vortex like structures can be observed, each with lengthscale comparable to a blade passage. The disturbances seen in Fig. 15 are therefore believed to arise from these structures propagating relative to the rotors.

During the experiment in Part I, it was also shown that short lengthscale disturbances were present, which interacted with the rotor itself to generate cut-on acoustic waves (see Part I, Fig. 15). It is therefore of interest to investigate if such an acoustic source is present in the computation.

Initially it appears that, in Fig. 15, one small disturbance is shed for each blade, propagating in the absolute frame of reference at approximately 79% of shaft speed. This implies two waveforms of *identical* wavelength are moving relative to each other (blade and stall cell). This will result in a difference tone with mode order zero—i.e., purely axial waves (analogous to a siren). It is straightforward to show that, at this propagation speed, the two waveforms will “beat” at a frequency of 7.2 engine order (EO). This manifests itself in the calculation as a “piston like” oscillation in massflow at Rotor 1 inlet, as shown in Fig. 18. The oscillation persists for several revolutions until the stall cells merge, diminishing the intensity of zeroth order wave. The generation of successive axial wavefronts can also be seen in Fig. 15.

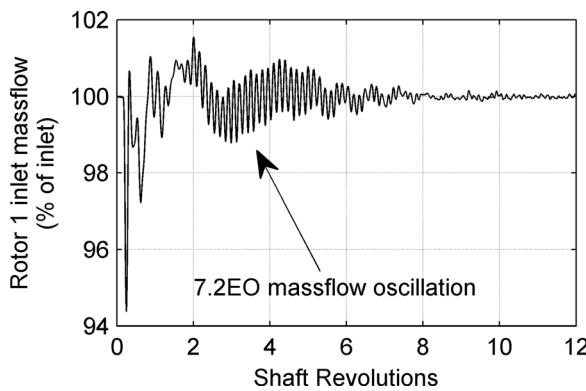


Fig. 18 Rotor 1 inlet mass flow during calculation

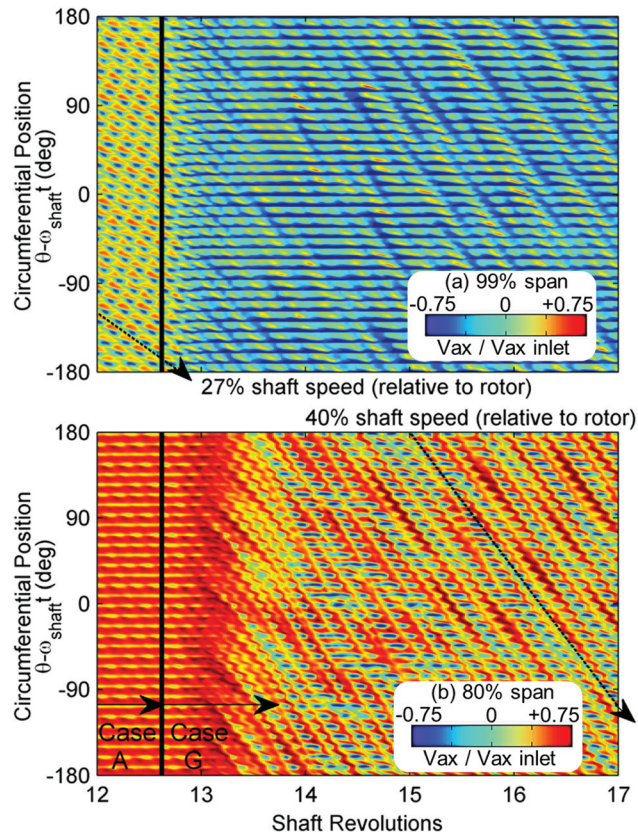


Fig. 19 Transient solution at R1 leading edge, (a) 99% span and (b) 80% span, when vanes are moved from case A to case G

Attention now turns to the development of this phenomenon as the VSVs are adjusted to the more stalled case G (Fig. 3). Once the configuration A solution was stable at $12\frac{1}{2}$ revolutions (noting also that the hub stalling phenomena was also stable), the VSVs were moved to the case G position. Figure 19 shows how the flow in the outer span region develops in the rotating frame of reference.

At 99% span (Fig. 19(a)) the 27 short lengthscale disturbances are almost immediately engulfed by a rapid growth in blockage as the tip flow becomes axially reversed.

Shown beneath this (Fig. 19(b)) is the corresponding behavior at 80% span. Initially, the flow is periodic, corresponding to the rotor blades—implying that the rotating stall at 99% span is not felt this far inboard. As the flow becomes axially reversed at 99% span, propagating disturbances appear at 80% span. This implies that they have grown inboard from the tip. Furthermore, they have decelerated in the absolute frame to 60% of shaft speed.

The final case G solution at revolution 22 is shown in Fig. 20 in terms of the axial velocity upstream of Rotor 1 (Fig. 20(a)) and the λ_2 vortex parameter isosurface (Fig. 20(b)). Clear vortex like

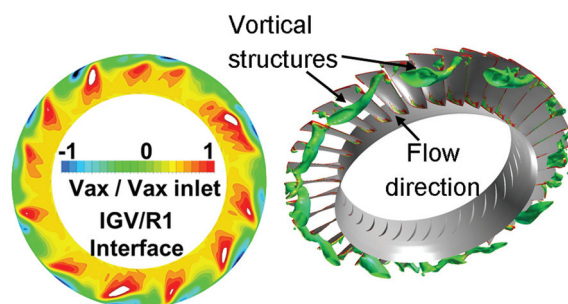


Fig. 20 Case G solution (a) axial velocity at IGV/R1 sliding plane and (b) isosurface of λ_2 parameter

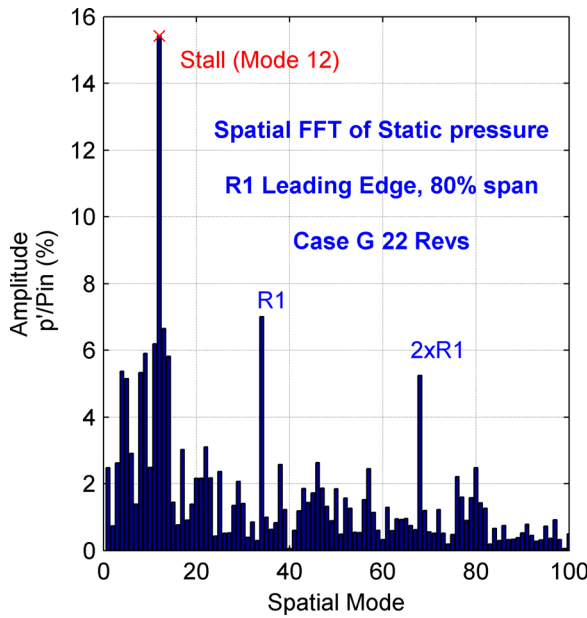


Fig. 21 Spatial modes (Rotor 1)—case G final

structures, now of greater circumferential lengthscale, can be observed with approximately 12 features identifiable around the circumference.

The spatial Fourier transform of this “final” fully developed solution is shown in Fig. 21, derived from the circumferential profile of static pressure at Rotor 1 leading edge, 80% span. The dominant circumferential mode implies 12 stall cells are present, consistent with the contour plot in Fig. 20(a). The associated static pressure variation is over twice the intensity of the Rotor 1 blade alone signal.

Performing the same modal analysis across chosen points in the computational domain allows the axial and radial distribution of the 12th spatial mode to be evaluated. Once again, this is limited to disturbances in static pressure. Fig. 22 shows this distribution along the hub and casing. The amplitude is of highest intensity toward the casing in the IGV/Rotor 1 gap. Upstream, the static pressure variation is attenuated almost completely by the IGV. This

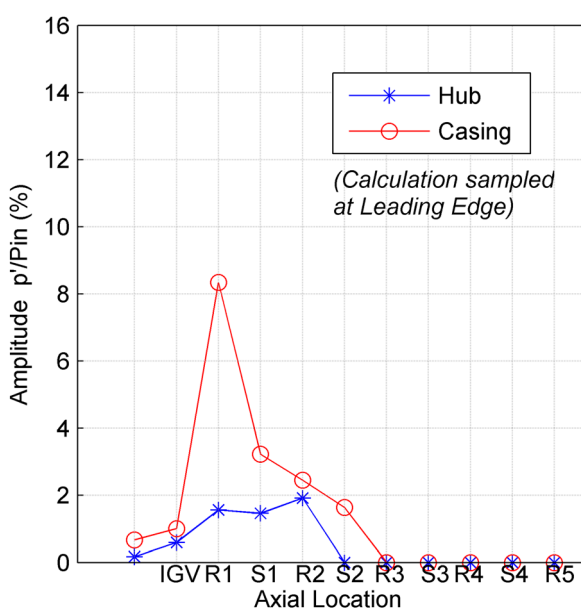


Fig. 22 Case G—distribution of 12th mode

most likely occurs because the IGVs are accelerating (nondiffusing) vanes, which cannot stall in response to the variation in exit static pressure. For this reason, the stall cells are limited in terms of their axial growth as they cannot extend into the IGV passages.

Comparison With Experiment. It is now possible to relate the behavior observed in the model back to the experimental observations presented in Part I.

For configuration A, very short length scale rotating stall was observed during the experiment at 85% shaft speed, with circumferential mode orders between 23 and 29 (this could be seen in Part I, Fig. 9, labeled “A1”). These disturbances propagated at approximately 65% of shaft speed *in the absolute frame*. The overall intensity of this signal was below 1% of inlet total pressure, when measured using a transducer in the IGV-Rotor 1 gap.

The simulation for configuration A shows good agreement in terms of the circumferential length scale of the rotating disturbances, with mode 27 apparent in the model. The predicted speed of 73% of shaft speed is also in agreement with experiment. The predicted amplitude of the resulting static pressure perturbation at Rotor 1 leading edge was 6% of inlet total pressure (see Fig. 16), falling to 0.2% by IGV exit, consistent with exponential decay of a cut-off disturbance. The predicted level is therefore in line with experiment, although this rapid decay implies that the measurement is highly sensitive to the location of the transducer, thus making such comparisons prone to error.

For the more stalled configuration G, spectral analysis in Part I showed that, at 85% shaft speed, mode order 15 was dominant, propagating at 55% of the shaft speed in the absolute frame of reference (Part I, Fig. 12). The existence of multiple frequency bands also suggested that some level of spatial and temporal nonuniformity was present. In comparison, the model shows that a 12 cell pattern is present, rotating at 60% of shaft speed. Spatial nonuniformity can be seen in Fig. 20(a), in contrast with the highly uniform hub stalling behavior seen earlier in Fig. 8. Scattering to adjacent spatial modes can also be observed in Fig. 21, also indicative of nonuniformity.

Taking the comparison further, the predicted intensity of spatial mode 12 is compared with experimental data for mode 15 in Fig. 23, at each measurement location. Experimental data is shown at both 85% and 86% speed, the latter speed included as the signal peaked sharply there. The agreement between experiment and

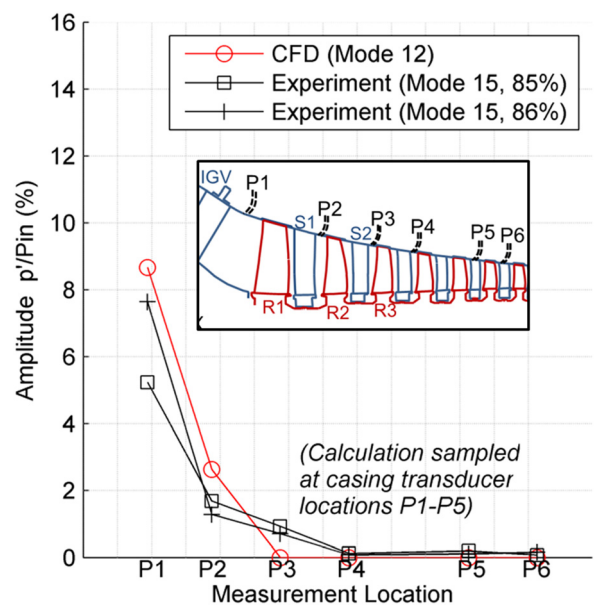


Fig. 23 Axial distribution of case G stalling mode—comparison with experiment

model is good, in terms of both the absolute level and axial distribution.

In summary, this section shows that as the VSVs are adjusted to push Rotor 1 toward stall (by opening the IGV and closing the downstream vanes), rotating stall cells form in the tip region. Initially these have very short lengthscale similar to that of a blade passage, which grow and merge as the rotor loading is increased further. These findings are consistent with the experimental observations.

Discussion

Having demonstrated that the numerical model gives credible predictions, the discussion now focuses upon whether any more insight can be gained into the observations made in experimentally in Part I.

The experimental findings in Part I showed quite clearly that, for the family of rotating stall linked to Stator 1/Rotor 2, the stall cell count appeared to spontaneously change several times during the acceleration maneuver (Part I, Fig. 7). Of particular interest, the propagation speed always *increased* when the cell count reduced (the cells growing in lengthscale). This observation is supported by the numerical behavior in Fig. 9, which show that as 7 cells grow and merge into 5, they also accelerate from 25% to 40% of shaft speed (in the absolute frame).

This observation would at first sight appear to be contrary to past experience. During stall inception, for example, spike disturbances initially appear at high propagation speed and decelerate as they grow in size [2]. In the majority of these cases, however, it is the rotor tip which becomes unstable, causing spikes (or embryonic stall cells of very short lengthscale) to come into existence in the rotating frame of reference, accelerating *relative to the rotor* as they grow.

This numerical investigation demonstrates that, for the Stator 1/Rotor 2 family, the disturbance forms *in the stator* (Fig. 10) and remains in this region as it grows to full size, with a much weaker presence in the neighboring blade rows (Fig. 12). It is therefore appropriate in this case to define stall propagation speed *relative to the stator*.

Consequently, it follows that, for short lengthscale cells, the predictions are entirely consistent with past experience when an appropriate relative propagation speed is used. The vast majority of reported cases involve spike formation in the rotor tip. However, spikes forming near the leading edge of shrouded diffuser vanes have been reported in a centrifugal compressor [16], rotating at only 20% of shaft speed.

It is also worth extending this discussion to the Rotor 1 stall family. Figure 19 shows that, now in the rotor frame of reference, the stall cells at Rotor 1 tip also accelerate as they grow in size. Once again, this remains consistent with the foregoing discussion and is more akin to the commonly reported cases of rotor tip stall.

The numerical results also show, in Fig. 8, that rotating stall forms in the *hub* region, persisting there as a stable disturbance. Again, this is not commonly reported. However, it is entirely possible for the hub to become unstable before the tip does. This is due to the relative change in the shape of the velocity triangles at the hub and tip, causing the loading at the hub to rise more rapidly than that at the tip, as the compressor is throttled [18].

Conclusions

In this paper the behavior of stable part span rotating stall in a multistage high speed compressor was investigated numerically at a fixed speed, by deliberate mis-staggering of the VSVs. Two clear families of rotating stall are predicted by the model.

As the Stator 1/Rotor 2 region was pushed into stall, multiple part span cells formed in the hub region of Stator 1. These subsequently grew in lengthscale both axially and circumferentially until the model stabilized on a pattern of 7 cells. Further throttling of this region caused these cells to grow and merge into 5 cells. The propagation speed of the stall pattern, in the absolute frame

of reference, increased as the disturbances grew. Comparison with experimental data showed that this prediction was credible, with the lengthscale, propagation speed, and intensity of the stall cells comparable to measurements.

As Rotor 1 was pushed into stall, part span stall cells formed in the tip region with very short lengthscale—comparable to that of a blade passage. These disturbances interacted with the rotor itself to generate 1D planar waves, causing the massflow to oscillate. Further throttling of this region caused these stall cells to grow and merge into a nonuniform pattern of stall cells with a dominant mode order of 12. The circumferential propagation speed of the stall pattern, in the *rotating* frame of reference, also increased as the stall cells grew. Once again, the predicted lengthscale, propagation speed, and intensity of the phenomenon were in good agreement with measurement.

Collectively, the numerical and experimental results offer important physical insights into the behavior of part span stall. First, it is shown that stall occurring in a row of stationary vanes is quite possible. Second, stall can form in the hub region, persisting there as a stable phenomenon.

Finally, this paper shows that unsteady RANS simulations are quite capable of predicting the detailed features of fully developed part span rotating stall. These disturbances could potentially couple with blade vibration modes or cause noise related issues, which can often not be identified during the design phase. The long-term trends toward both lighter weight components and more highly loaded aerodynamic design styles are likely to exacerbate this problem. From the point of view of a designer, therefore, an upfront prediction of the frequencies and amplitudes at which rotating stall is likely to occur is of significant long term benefit.

Acknowledgment

The authors wish to thank the Compressor Aerodynamics and Experimental Vibration groups at Rolls-Royce plc, together with contributions made by a number of individuals. These include N.A. Cumpsty of Imperial College, I. Day and C. Freeman, both of the Whittle Laboratory, for several useful discussions on this topic. The support of J. Green, S. Stapelfeldt and the staff at the Vibration UTC, Imperial College is also gratefully acknowledged. Finally, this work was made possible due to funding from the UK TSB TUFT (Turbomachinery Flow and Turbulence) program.

Nomenclature

CFD = computational fluid dynamics

CPU = central processing unit

EO = engine order

N = rotational speed of shaft (Hz)

p' = static pressure (pk–pk unsteady component)

P_{in} = inlet total pressure

T_{in} = inlet total temperature

U = blade speed

V_{ax} = axial velocity

V_{stall} = speed of propagation of stall cells

VSV = variable stator vane

References

- [1] Moore, F. K., and Greitzer, E. M., 1986, "A Theory of Post-Stall Transients in Axial Compression Systems—Parts I and II," *ASME J. Eng. Gas Turbines Power*, **108**(2), pp. 231–239.
- [2] Day, I. J., 1993, "Stall Inception in Axial Flow Compressors," *ASME J. Turbomach.*, **115**(1), pp. 1–9.
- [3] Camp, T. R., and Day, I. J., 1998, "A Study of Spike and Modal Stall Phenomena in a Low-Speed Axial Compressor," *ASME J. Turbomach.*, **120**(3), pp. 393–401.
- [4] He, L., 1997, "Computational Study of Rotating Stall Inception in Axial Compressor," *J. Propul. Power*, **13**(1), pp. 31–38.
- [5] Hoyer, D. A., Tan, C. S., Vo, H. D., and Greitzer, E. M., 1999, "Role of Blade Passage Flow Structures in Axial Compressor Rotating Stall Inception," *ASME J. Turbomach.*, **121**(4), pp. 735–742.

- [6] Gourdain, N., Burguburu, S., Leboeuf, F., and Miton, H., 2006, "Numerical Simulation of Rotating Stall in a Subsonic Compressor," *Aerosp. Sci. Technol.*, **10**(1), pp. 9–18.
- [7] Vahdati, M., Simpson, G., and Imregun, M., 2008, "Unsteady Flow and Aeroelasticity Behaviour of Aeroengine Core Compressors During Rotating Stall and Surge," *ASME J. Turbomach.*, **130**(3), p. 031017.
- [8] Choi, M., Vahdati, M., and Imregun, M., 2011, "Effects of Fan Speed on Rotating Stall Inception and Recovery," *ASME J. Turbomach.*, **133**(4), p. 041013.
- [9] Choi, M., Smith, N. H. S., and Vahdati, M., 2013, "Validation of Numerical Simulation for Rotating Stall in a Transonic Fan," *ASME J. Turbomach.*, **135**(2), p. 021004.
- [10] Gourdain, N., Burguburu, S., Leboeuf, F., and Michon, G. J., 2010, "Simulation of Rotating Stall in a Whole Stage of an Axial Compressor," *Comput. Fluids*, **39**(9), pp. 1644–1655.
- [11] Chen, J. P., Hathaway, M. D., and Herrick, G. P., 2008, "Prestall Behaviour of a Transonic Axial Compressor Stage via Time-Accurate Numerical Simulation," *ASME J. Turbomach.*, **130**(4), p. 041014.
- [12] Vo, H. D., Tan, C. S., and Greitzer, E. M., 2008, "Criteria for Spike Initiated Rotating Stall," *ASME J. Turbomach.*, **130**(1), p. 011023.
- [13] Pullan, G., Young, A., Day, I., Greitzer, E. M., and Spakovszky, Z. S., 2012, "Origins and Structure of Spike-Type Rotating Stall," *ASME* Paper No. GT2012-68707.
- [14] Everitt, J. N., and Spakovszky, Z. S., 2012, "An Investigation of Stall Inception in Centrifugal Compressor Vaned Diffusers," *ASME J. Turbomach.*, **135**(1), p. 011025.
- [15] Young, A., Day, I., and Pullan, G., 2011, "Stall Warning by Blade Pressure Signature Analysis," *ASME J. Turbomach.*, **135**(1), p. 01133.
- [16] Spakovszky, Z. S., and Roduner, C. H., 2009, "Spike and Modal Stall Inception in an Advanced Turbocharger Centrifugal Compressor," *ASME J. Turbomach.*, **131**(3), p. 031012.
- [17] Lieblein, S., Schwenk, F. C., and Broderick, R. L., 1953, "Diffusion Factor for Estimating Losses and Limiting Blade Loadings in Axial Flow Compressor Blade Elements," NACA Report No. RM E53D01.
- [18] Cumpsty, N. A., 1989, "Compressor Aerodynamics," *Longman Scientific and Technical*, Wiley, New York.